A Generalized View of Foam Drainage: Experiment and Theory

Stephan A. Koehler,* Sascha Hilgenfeldt, and Howard A. Stone

Pierce Hall, Division of Engineering & Applied Sciences, Harvard University, Cambridge, Massachusetts 02138

Received October 5, 1999. In Final Form: February 23, 2000

A new experimental method is presented using fluorescein dye to determine the spatial and temporal variations of the liquid volume fraction in aqueous foams. This method is used for quantitative studies of liquid redistribution (*drainage*) in three types of experiments: forced, free, and pulsed drainage. Characteristic quantities, such as the drainage velocity, show power-law dependences on experimental parameters that are inconsistent with traditional foam drainage models based on Poiseuille-type flow in the liquid-carrying channels (Plateau borders) of the foam. To obtain a theoretical description, the *foam drainage equation* is generalized using an energy argument which accounts for viscous dissipation in both the channels and the nodes (or vertices, which are the junctions of four channels) of the liquid network. Good agreement with results for all three types of drainage experiments is found when using this new model in the limit where the dissipation is dominated by the nodes.

1. Introduction

There are many industrial as well as everyday uses for foams in either liquid or solid form. Aqueous foams are ubiquitous in the kitchen: examples are whipped cream, chocolate mousse (N.B. mousse is the French word for foam), beer foam, and soapy dish water. Polymeric foams have numerous applications such as seat cushions and packaging (e.g. Styrofoam). Recently there has also been interest in foaming metal melts to produce metallic foams, which are useful in many mechanical applications because of their structural stability and ultralight weight. These foams have recently come into use in the aerospace and automotive industries.[1,2]

Many foams are made by introducing bubbles into a liquid which contains a surfactant in order to stabilize the gas/liquid interfaces. The spatial and temporal liquid distribution is governed by the fluid dynamics of the liquid in the foam. Under the influence of gravity liquid will *drain* from the foam and accumulate at the bottom, leaving the top deprived of liquid. Such an inhomogeneity of liquid content may be undesirable in applications such as the aforementioned structural metal foams. It is unclear how the dynamics of fluid flow varies for different kinds of foams: Is there a simple description of fluid transport through foams that is universally applicable to different situations and different foams? Do different foams have different boundary conditions at the gas/liquid interface? In particular, how does the presence of a surfactant affect the boundary conditions? Even the fluid dynamics of aqueous (soap) foams, which are the simplest and easiest system to study, is poorly understood.[3−5] Here we report new results for three types of drainage experiments for aqueous foams, along with a modification to the existing foam drainage model that succeeds in capturing the features of liquid drainage in all of these cases.

Foam drainage is the flow of liquid through the interstitial spaces between the bubbles. The flow is driven by capillarity and (usually) gravity and is resisted by viscous damping.[6−9] The interstitial space, i.e., the liquid volume, can be divided into (i) *films*, which form between two adjacent bubbles and are bounded by almost flat bubble faces, (ii) *channels* (also known as *Plateau borders*), where three films meet, and (iii) *nodes* (also known as *vertices* or *junctions*), where four channels meet (see Figure 1b). On the scale of single bubbles the flow is rather intricate: for example in the nodes flows from different channels merge and subsequently split into flows through other channels. The dynamics is further complicated by the flow along the gas/liquid interface; e.g., are the surfaces rigid or mobile? In spite of this small-scale complexity, on a *macroscopic* scale (i.e. lengths of at least several bubble diameters) simple ordered flow is often observed and it is possible to successfully describe foam drainage using effective-medium models.

There are other processes that can change the macroscopic appearance of a foam, in particular *coarsening*, which refers to the growth of the average bubble size. This can occur either by film rupture (coalescence of adjacent bubbles) or by diffusive coarsening, where large bubbles grow at the expense of smaller bubbles, whose higher capillary pressure makes them lose gas. This latter effect is similar to the process known as Ostwald ripening of metal grains.[10] With a good surfactant, films are very stable and rupture events occur only rarely. Diffusive coarsening will always be important at long enough times; however, in the experiments reported here we have taken countermeasures to avoid coarsening.

* To whom correspondence should be addressed. E-mail: skoehler@deas.harvard.edu.

(1) Gibson, L. J.; Ashby, M. F. *Cellular Solids*; Cambridge University Press: Cambridge, U.K., 1997.
(2) Evans, A. G.; Hutchinson, J. W.; Ashby, M. F. *Curr. Opin. Solid State Mater.* **1998**, *3*, 288−303.
(3) Desai, D.; Kumar, R. *Chem. Eng. Sci.* **1982**, *37*, 1361.
(4) Kraynik, A. M. Sandia National Laboratories, Internal Report, 1983; 83-0844.
(5) Koehler, S. A.; Hilgenfeldt, S.; Stone, H. A. *Phys. Rev. Lett.* **1999**, *82*, 4232.
(6) Bikerman, J. J. *Foams*; Springer: New York, 1973.
(7) Leonard, R. A.; Lemlich, R. *AIChE J.* **1965**, *11*, 18.
(8) Weaire, D.; Hutzler, S.; Verbist, G.; Peters, E. *Adv. Chem. Phys.* **1997**, *102*, 315.
(9) Bhakta, A.; Ruckenstein, E. *Adv. Colloid Interface Sci.* **1997**, *70*, 1−124.
(10) Smith, C. S. Grain Shapes and other Metallurgical Applications of Topology. In *Metal Interfaces*; Herring, C., Ed.; American Society for Metals: Cleveland, OH, 1952; p 65.

10.1021/la9913147 CCC: $19.00
Published on Web 06/30/2000

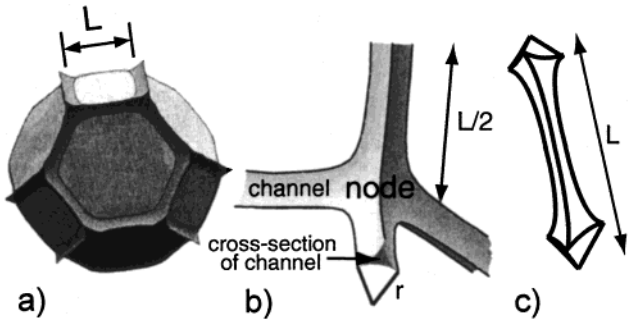

Figure 1. (a) Tetrakaidecahedral bubble with liquid-filled channels and nodes, with edge length L, that composes an idealized Kelvin foam (reproduced from a figure by A. Kraynik, private communication). A liquid network unit composed of one node and four half-channels with corresponding volume fraction $\epsilon = 0.005$ is shown in (b). A "dog-bone"-shaped liquid network unit, one channel with one-quarter-node at each end, is sketched in (c). (a) and (b) have been generated using the Surface Evolver.[27]

In the past, researchers have focused on a variety of aspects of soap foams. The 19th century Belgian scientist J. A. F. Plateau, at a time when he was already blind, originated the study of soap foams, mainly investigating their geometry. He formulated "Plateau's rules", which state that three films must meet at 120° angles and four channels at the tetrahedral angle of $\arccos(-1/3) \approx 109.5°$, and also the eminent minimal surface problem known as the Plateau problem.[11,12] The reader interested in the large body of foam research spanning physical chemistry and engineering applications is referred to the monographs by Mysels et al.[13] and Bikerman[6] and the recent compilation by Prud'homme and Khan[14] as well as the proceedings edited by Sadoc and Rivier.[15]

We are particularly interested in simple dynamical models for foam drainage. Research in this spirit appears to begin with the work of Leonard and Lemlich,[7] who performed foam drainage experiments and developed a model based upon balancing gravity and viscous effects for a Poiseuille-type flow in the channels. Kraynik found analytical solutions to this model for the case of negligible surface tension.[4] The attempt to remove the effects of surface tension recently led Durian and co-workers to perform drainage experiments using a clever geometry of the foam container[16] (earlier publications[17,18] also treat container shape effects on drainage). Reintroducing surface tension into the description of drainage, Goldfarb et al. developed what is now called the *foam drainage equation*.[19] This theory was supported by systematic experiments performed in Weaire's group several years later,[20] who also presented an independent reformulation of the foam drainage equation. However, already Desai and Kumar[3] and Kraynik[4] remarked that the basic assumptions of this standard model lead to slower drainage rates than those observed in their experiments. In recent work, we proposed a modification to the model, based upon the nodes of the liquid network as the principal region of dissipation. This modified model agrees well with data from our forced drainage experiments.[5] Very recently Langevin and co-workers found that changing the surface viscosity of a SDS (sodium dodecyl sulfate) solution by adding dodecanol affects the drainage rates, and for SDS alone their forced drainage results agree with ours.[21] Further evidence that changing the interfacial chemistry significantly alters the drainage rate is provided by Wilde et al.,[22] who report that foams stabilized by proteins drain much slower than foams stabilized by low molecular weight surfactants, such as SDS.

In this paper, we treat the two different models as limiting cases of a generalized theory and demonstrate that the theory which focuses on dissipation in the nodes[5] is in close agreement with data for a variety of drainage experiments. The remainder of this section details the geometry of foams and presents the main ideas of a foam drainage theory, while section 2 describes the experimental setup and methods, along with the main results of the measurements. In sections 3 and 4 a generalized foam drainage equation is derived and discussed and compared to the experimental results. Concluding remarks are given in section 5.

1.1. Foam Geometry. The surfaces of the bubbles of aqueous foams are coated with surfactants which are necessary to stabilize the films against rupture by providing a disjoining pressure (electrostatic and steric in nature) that keeps opposing faces from merging.[23] Outside of the film regions, the dominant force determining the foam geometry is surface tension, which acts to minimize the surface area of the bubbles and results in constant mean curvature.

One simple idealized foam structure is the Kelvin foam,[24] which is a collection of regular tetrakaidecahedral bubbles (cells) with edge length L (see Figure 1a and e.g. Princen[25]). The maximum dimension of a cell is approximately 2.8 L. Typical film thicknesses of the faces of aqueous foams are $\lesssim$ 100 nm,[26] so that most of the liquid resides in the channels and nodes, which are typically between 10 μm and 1 mm wide. Here the contact angle between two channel walls meeting at a face is assumed to be vanishingly small, and the liquid content of the face (and thus the film thickness) is assumed zero. As the amount of liquid in the channels and nodes increases, the mean curvature of the interfaces decreases, and the edges and corners of the polygonal bubbles become more rounded. We quantify the liquid content of a foam by the *liquid volume fraction* ϵ, defined as the volume of liquid in a macroscopic foam region divided by the total volume of the region.

(11) Plateau, J. A. F. *Statique expérimentale et théorique des liquides soumis aux seules forces moléculaires*; Gauthier-Villars, Trubner et cie: Paris, 1873.
(12) Isenberg, C. *The Science of Soap Films and Soap Bubbles*; Dover: London, 1992.
(13) Mysels, K. J.; Shinoda, K.; Frankel, S. *Soap Films, studies of their thinning*; Pergamon Press: London, 1959.
(14) Prud'homme, R. K., Khan, S. A., Eds. *Foams, Theory, Measurements and Applications*; Marcel Dekker: New York, 1996.
(15) Sadoc, J. F., Rivier, N., Eds. *Foams and Emulsions*; Kluwer Academic: Dordrecht, The Netherlands, 1997.
(16) Saint-Jalmes, A.; Vera, M. U.; Durian, D. J. *Euro. Phys. J. B* **1999**, *12*, 67−73.
(17) Princen, H. M. *J. Colloid Interface Sci.* **1990**, *134*, 188.
(18) Narsimhan, G.; Ruckenstein, E. Structure, Drainage, and Coalescence of Foams and Concentrated Emulsions. In *Foams, Theory, Measurements and Applications*; Prud'homme, R. K.; Khan, S. A., Eds.; Marcel Dekker: New York, 1996; p 99.
(19) Goldfarb, I. I.; Kann, K. B.; Shreiber, I. R. *Fluid Dyn.* **1988**, *23*, 244.
(20) Verbist, G.; Weaire, D.; Kraynik, A. *J. Phys. Condens. Matter* **1996**, *8*, 3715−3731.
(21) Durand, M.; Martinoty, G.; Langevin, D. *Phys. Rev. E* **1999**, *60*, R6307.
(22) Wilde, P. J.; Mackie, A. R.; Husband, F. A.; Gunning, A. P.; Morris V. J.; Fillery-Travis, A. The Role of Interfacial Structure and Composition on Foam Drainage and Fluid Dynamics. In *Foams and Films: Proceedings of the International Workshop on Foams and Films, Leuven, Belgium*; Weaire, D., Banhart, J., Eds.; MIT-Verlag: Bremen, Germany, 1999; p 59.
(23) Adamson, A. W. *Physical Chemistry of Surfaces*; Wiley: New York, 1990.
(24) Kelvin, L. *Philos. Mag.* **1887**, *24*, 503.
(25) Princen, H. M. *Langmuir* **1986**, *2*, 519.
(26) Wasan, D. T.; Nikolov, A. D.; Lobo, L. A.; Kozco, K.; Edwards, D. A. *Prog. Surf. Sci.* **1992**, *39*, 119.

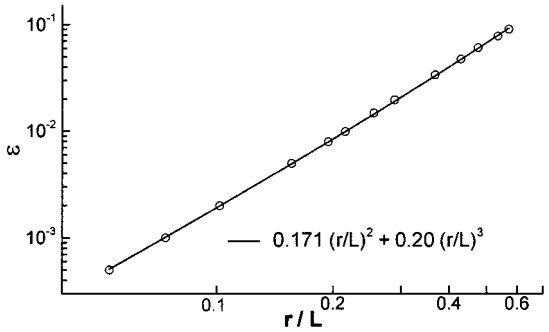

Figure 2. Liquid volume fraction ϵ of the idealized Kelvin foam versus r/L as computed (○) by the Surface Evolver[27] in the absence of gravity. The solid line is the polynomial fit (1) which is in excellent agreement with the numerical data.

To arrive at a geometrical description of the channel network (no faces) we consider the equilibrium situation without gravity, where the mean curvature H is constant. The two principal radii of curvature r_1 and r_2 will change from point to point, obeying $2H = r_1^{-1} + r_2^{-1}$. We define the *characteristic radius of curvature* r by $r^{-1} = 2H$ and plot ϵ as a function of r in Figure 2. The points are computed for the idealized tetrakaidecahedral foam using the Surface Evolver,[27] and the solid line is a fit to the formula

$$\epsilon = \delta_\epsilon\left(\frac{r}{L}\right)^2 + \delta'\left(\frac{r}{L}\right)^3 \qquad \delta_\epsilon \approx 0.171 \qquad \delta' \approx 0.20 \qquad (1)$$

Since here we are principally concerned with the dry foam limit, corresponding to $\epsilon \ll 1$, we have $r \ll L$, and the approximation

$$r \approx \delta_\epsilon^{-1/2} L \epsilon^{1/2} \qquad (2)$$

is good for liquid volume fractions $\epsilon \lesssim 0.1$.

There is a simple geometrical justification for the polynomial fit (1). Foams with low liquid content ($\epsilon \lesssim 0.05$) have channels that are long, essentially straight, and slender, containing much more liquid than the nodes. With decreasing ϵ the channel length approaches L and the transverse radius of curvature of the channel approaches r from above because the longitudinal radius of curvature becomes large. The cross-sectional area of a channel approaches $\delta_a r^2$, with $\delta_a = \sqrt{3} - \pi/2$, which is the area between three contiguous circles of radius r (see Figure 1b). If one neglects small overlap regions in the junctions, the liquid content of a tetrakaidecahedral bubble is $12\delta_a r^2 L$ because there are 12 complete channels per bubble. The volume of the tetrakaidecahedron[1] is $2^{7/2}L^3$, so the liquid volume fraction due to the channels is $12\delta_a 2^{-7/2}(r/L)^2 \approx 0.171(r/L)^2$, which is the first term on the right-hand side of (1). Higher-order corrections arise from the presence of nodes which (i) diminish the length of the channels by $O(r)$ and (ii) introduce a node volume $v_n = \delta_n r^3$, with $\delta_n = O(1)$.[28] This leads to the δ' term in (1), the only genuine fit parameter in the equation.[29] For foams with low liquid content, however, the channels account for almost all of the liquid, and we will neglect node corrections to the volume.

1.2. Foams as Porous Media. It is useful to consider an analogy between the drainage of a foam and the flow of liquid through a porous medium such as sand or a packed bed of rigid spheres.[30,31] The dimensions and number density of the connected pores determine the permeability of the porous medium to liquid flow. Darcy's law relates the driving pressure gradient $\mathbf{G}$ to the permeability k and the average liquid velocity through the medium $\mathbf{v}$,

$$\mathbf{G} = -\nabla p + \rho\mathbf{g} = \mu\mathbf{v}/k \qquad (3)$$

where μ is the viscosity, p is the liquid pressure, and $\rho\mathbf{g}$ is the gravitational force. Permeability has dimensions of length squared and scales with the square of a characteristic pore size. For foams the interstitial space between the bubbles (channels and nodes) plays the role of the pores through which liquid can pass. However the interstitial space (i.e. volume fraction) of a foam is not fixed and bubble deformation accompanies liquid flow. Thus unlike conventional porous media, foams have a permeability that is dynamically coupled to the liquid flux.

Note that eq 3 is *macroscopic* in the sense that all quantities (e.g. the gradient) are averaged over length scales larger than a pore size. Unless explicitly denoted "microscopic", all quantities will be understood as macroscopic, describing foam drainage on an effective-medium level.

1.3. The Generalized Foam Drainage Equation. We seek to describe the spatial and temporal dynamics of the liquid volume fraction, $\epsilon(\mathbf{x}, t)$. Inertial terms can be neglected, as we estimate that the Reynolds numbers of liquid flow, based upon a typical channel radius, are never larger than 10 and in most cases are much smaller than 1. The discussion below is a modified presentation of Koehler, Hilgenfeldt, and Stone[32] and has many features in common with previous models.[19,33]

A suitable starting point is the equation of mass conservation,

$$\frac{\partial\epsilon}{\partial t} + \nabla\cdot(\epsilon\mathbf{v}) = 0 \qquad (4)$$

in which $\mathbf{v}$ (see (3)) is the macroscopic velocity of the flow through the foam. On the left-hand side of (3), the liquid pressure p is given by the Young−Laplace equation

$$p = p_{gas} - \gamma/r \qquad (5)$$

where γ is the surface tension. The foam is assumed monodisperse, so all of the bubbles have the same gas pressure p_{gas}, as well as the same volume, because the weight of the foam is small and compression due to gravity is negligible.[8]

With (2) and (5) the driving force $\mathbf{G}$ from (3) becomes

$$\mathbf{G} = \rho\mathbf{g} + \nabla(\gamma/r) \approx \rho\mathbf{g} + \frac{\gamma\delta_\epsilon^{1/2}}{L}\nabla\epsilon^{-1/2} \qquad (6)$$

We use (3) and (6) to solve for $\mathbf{v}$ in terms of ϵ and the permeability $k(\epsilon)$ and substitute this into (4) to arrive at the *generalized foam drainage equation*

(27) Brakke, K. Univ. of Minnesota Geometry Center, Surface Evolver Version 2.10c; http://www.geom.umn.edu.

(28) The prefactor δ_n for the node volume can be estimated assuming that the geometrical shape of the nodes resembles that of the interstitial space between hexagonally close-packed spheres (which is the structure of a wet foam with spherical bubbles). The packing fraction of the fcc structure is $\sqrt{2}\pi/6 \approx 0.74$, and each sphere has $^{14}/_4$ complete nodes. This yields $\delta_n \approx 0.31$.

(29) Phelan, R.; Weaire, D.; Peters, E.; Verbist, G. J. Phys. Condens. Matter **1996**, *8*, L475.

(30) Zick, A. A.; Homsy, G. M. *J. Fluid Mech.* **1982**, *115*, 13.

(31) Larson, R. E.; Higdon, J. J. L. *Phys. Fluids A* **1989**, *1*, 38.

(32) Koehler, S. A.; Hilgenfeldt, S.; Stone, H. A. Foam Drainage: Experiments and a New Model. In *Foams and Films: Proceedings of the International Workshop on Foams and Films, Leuven, Belgium*; Weaire, D., Banhart, J., Eds.; MIT-Verlag: Bremen, Germany, 1999; p 49.

(33) Weaire, D.; Phelan, R. *J. Phys. Condens. Matter* **1996**, *8*, 9519.

$$\mu\frac{\partial\epsilon}{\partial t} + \rho\mathbf{g}\cdot\nabla(k(\epsilon)\epsilon) - \frac{\gamma\delta_\epsilon^{1/2}}{L}\nabla\cdot(k(\epsilon)\nabla\epsilon^{1/2}) = 0 \qquad (7)$$

It remains to compute the foam permeability in terms of ϵ. A detailed derivation of a general expression for $k(\epsilon)$ will be presented in section 3. Here, we give a simple argument for the functional form of $k(\epsilon)$ in the two limiting models of foam drainage.

The original foam drainage model is based upon rigid gas/liquid interfaces, which cause Poiseuille-like flow in the channels.[19,20] The viscous damping force (per unit volume) in the channels then is $O(\mu v' r^{-2})$, where v' is a characteristic liquid velocity which is on the order of the macroscopic liquid velocity. For dry foams the node volume is negligible (cf. (1)), and so the viscous damping of the liquid flow is dominated by the channels. Since the Reynolds number is small, the viscous damping equals the driving force from Darcy's law (cf. (6)), and it follows from $\mu v/k(\epsilon) \propto \mu v' r^{-2}$ that $k(\epsilon) \propto r^2 \propto L^2\epsilon$. To differentiate from other models, we call this the *channel-dominated model*.

An alternative boundary condition stipulates that the gas/liquid interface is not rigid but rather freely slipping and stress-free.[5] Although the flow in the nodes may be very complicated due to the mixing and bending of the flow (see Figure 1b), the viscous damping force (per unit volume) inside the nodes is $O(\mu v' r^{-2})$, because r is the only length scale of the nodes. Inside the channels however the viscous damping is negligible, because there the flow is pluglike and the velocity gradients are small. Hence the nodes dominate the dissipation, and we shall call this the *node-dominated model*. Thus the *average* damping force over a network structure is given by $O(\mu v' r^{-2}(r/L))$, because the ratio of the node volume to the volume of the network is $O(r/L)$. Equating the net damping force to the term $\mu v/k(\epsilon)$ of Darcy's law (3) yields $k(\epsilon) \propto rL \propto L^2\epsilon^{1/2}$.

2. Foam Drainage Experiments

In the following we briefly describe the experimental techniques we use to measure the liquid volume fraction of draining foams, which differ from previous work[7,34,35] in several respects. We then review the three different types of foam drainage experiments that we have studied in detail: *forced*, *free*, and *pulsed drainage*.[20] In this section, we present the main results of the measurements. An extensive analysis of the drainage dynamics is deferred to section 4.

2.1. Experimental Procedure. To study foam drainage experimentally we have developed a new measurement scheme and a new procedure to produce a uniform, nearly monodisperse foam that does not show signs of coarsening.[5] The foam is inside a vertical Tygon tube that is 2 m long and has a diameter of 1.3 cm (see Figure 3). The bottom of this *foaming tube* is inserted into a vessel containing the soap solution, and a slow flow of C_2F_6 gas through a blunt-end syringe needle produces a constant supply of monodisperse bubbles, filling the tube at a rate of 0.025 cm/s. At the top the foam flows out of the Tygon tube into a catch basin about 1 m above the experimental region of interest.

The foaming solution is composed of single-distilled water, SDS surfactant (sodium dodecyl sulfate), and fluorescein salt in the ratio of 1 to 5×10^{-3} to 2.5×10^{-4} by weight. The corresponding molarity of SDS is 0.017 M, which is well above the critical micelle concentration (CMC) of this surfactant.[36] The results were unchanged when the soap concentration was either doubled or halved. SDS is a surfactant whose properties are well-known and which is readily available in purified form. The findings reported in the present work support earlier experiments with Dawn dish detergent, tap water, and air[5] and show that the drainage behavior seems to be robust toward these changes. We also conducted some experiments using the surfactant AOS (α-olefinsulfonate), with essentially unchanged results.

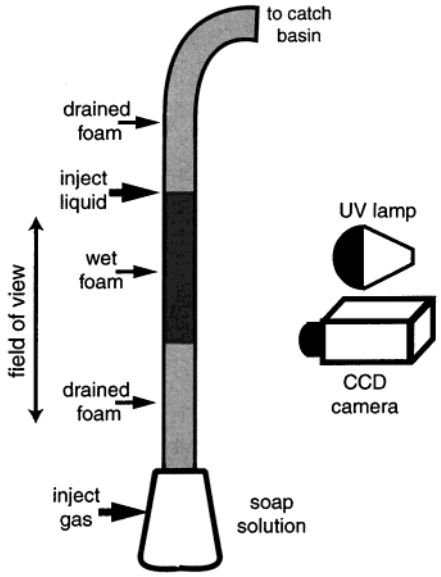

Figure 3. Schematic of the experimental setup, here showing forced drainage. Liquid is injected into the foaming tube at a constant rate above the field of view of the CCD camera. This produces a growing region of wet foam in the otherwise well-drained foam. The CCD camera records the fluorescence of the foam illuminated by UV light from which the liquid volume fraction in the foam can be deduced.

As a result of the slow bubbling, the foam inside the foaming tube is well drained and very *dry* ($\epsilon < 10^{-4}$). We chose C_2F_6 for bubbling, because this gas has a low diffusion coefficient and a low saturation level in water which minimizes coarsening. The bubble size was determined from a close-up photograph of the foam, and the average edge length is $L = 0.15$ cm with a standard deviation of 0.04 cm. The foam does not age or coarsen with time, when observed at a fixed height in the tube, because it is continually being replenished from the bottom. The edge length L does not vary noticeably over the region of observation, which is 76 cm high and starts 40 cm above the foaming solution.

The actual foam drainage experiments record the dynamics of excess liquid added to the well-drained foam. This excess liquid is the same soap solution described above and is injected into the foam through a syringe needle inside the foaming tube. A programmable syringe pump was used for the injection process, and the amount of liquid actually dispensed was independently checked with digital calipers.

2.2. Fluorescence Measurements. The experimental measurements use UV light to excite fluorescence in the liquid part of the foam. The small amount of fluorescein salt dissolved in the foaming solution absorbs the illuminating UV radiation and emits visible (yellow-green) light. The fluorescence intensity, recorded by a CCD digital camera, with a green light filter mounted, is thus a measure of liquid content. Consider a UV light ray that passes through the foam, which has a total path length H in the foam and intensity $I_{UV}(h)$, where $h \le H$ is the distance traversed. The attenuated intensity is $I_{UV}(h) = \exp(-\alpha_{liq}\epsilon h)$, where α_{liq} is the UV absorption coefficient (inverse of absorption length) of the fluorescein solution. We assume that the emission of visible light from the fluorescein occurs isotropically and that for small ϵ the visible light is not reabsorbed noticeably, making the total detected fluorescence intensity

$$I \propto 1 - \exp(-\alpha_{liq}\epsilon H) \qquad (8)$$

so that a linear relation $I \propto \epsilon$ between detected intensity and

(34) Weaire, D.; Pittet, N.; Hutzler, S.; Pardal, D. *Phys. Rev. Lett.* **1993**, *71*, 2670.

(35) Weaire, D.; Findlay, S.; Verbist, G. *J. Phys. Condens. Matter* **1995**, *7*, L217.

(36) Prud'homme, R. K.; Warr, G. G. Foams in Mineral Flotation and Separation Processes. In *Foams, Theory, Measurements and Applications*; Prud'homme, R. K., Khan, S. A., Eds.; Marcel Dekker: New York, 1996; p 511.

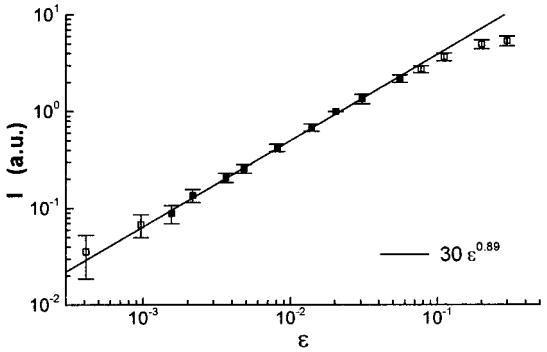

Figure 4. Forced drainage fluorescence intensity plotted against main body liquid volume fraction, determined from eq 10. The line shows the best fit to power-law behavior; see eq 9. The open squares were not included in the power-law fit.

volume fraction is valid if $\alpha_{liq}\epsilon H \ll 1$, and the intensity saturates ($I \rightarrow I_{max}$) for $\alpha_{liq}\epsilon H \gg 1$.

An independent measurement of liquid volume fraction is possible when performing a forced drainage experiment, as described in section 2.3. Figure 4 shows that the relationship between I and ϵ for $\epsilon \lesssim 0.05$ is close to linear in an extended range of liquid volume fractions. A small deviation is, however, evidenced by the best-fit power law

$$I \propto \epsilon^{0.89} \tag{9}$$

which we attribute to a slight nonlinearity of the camera response. From the range of approximate linearity in Figure 4 and using eq 8, we estimate $\alpha_{liq}^{-1} \approx 0.5$ mm, which is comparable to the liquid path lengths ϵH in our experiments, where H is the diameter of the foaming tube.

Data points at large $\epsilon \gtrsim 0.1$ were not used for the fit because of the saturation of the fluorescence. Also, two data points at extremely small $\epsilon \lesssim 10^{-3}$ were excluded as these very faint signals cannot be detected with reasonable accuracy.

2.3. Forced Drainage. In the forced drainage experiment, a constant flux of the soap solution is added at the top of the foaming tube (about 20 cm above the field of view of the camera), and the liquid invades the completely drained foam from above. The measured volume fraction profiles at five successive times in Figure 5a show a *drainage wave* making its way down the foam tube. It is observed that all forced drainage profiles have a distinct front that does not change in shape with time and moves downward with a constant velocity v_f, thus forming a solitary wave. Because the foam is generated at the bottom at a constant rate, it is necessary to add the (very slow) speed at which the foam rises to the measured downward front velocity of the drainage wave.

The forced drainage wave profile consists of three regions (see Figure 5a): the drained region below the traveling wave, which has very little liquid volume content ($\epsilon < 10^{-4}$), the transition (front) region, which has a characteristic width (typically several bubble diameters), and finally the *main body*, which has uniform volume fraction $\epsilon = \epsilon_{main}$. We choose to measure the front width as the vertical distance along the profile where ϵ drops from 80% to 20% of its main body value. In the experiments, both the front speed v_f and width w_f are measured as a function of the injected one-dimensional liquid volume flux Φ. Because of conservation of liquid volume, the flux through the foam is simply the product of the average macroscopic liquid velocity v and the main body liquid volume fraction ϵ_{main}; thus

$$\epsilon_{main} = \Phi/v \tag{10}$$

The liquid velocity of the forced drainage wave is the front velocity, $v = v_f$, because the profile maintains its shape—see Figure 5a. If the front traveled faster than the average liquid velocity, it would broaden, and if it were slower than the average liquid velocity, a steepening of the front would be observed.

Relation (10) allows for an independent calibration of fluorescence intensity measurements as mentioned in section 2.2

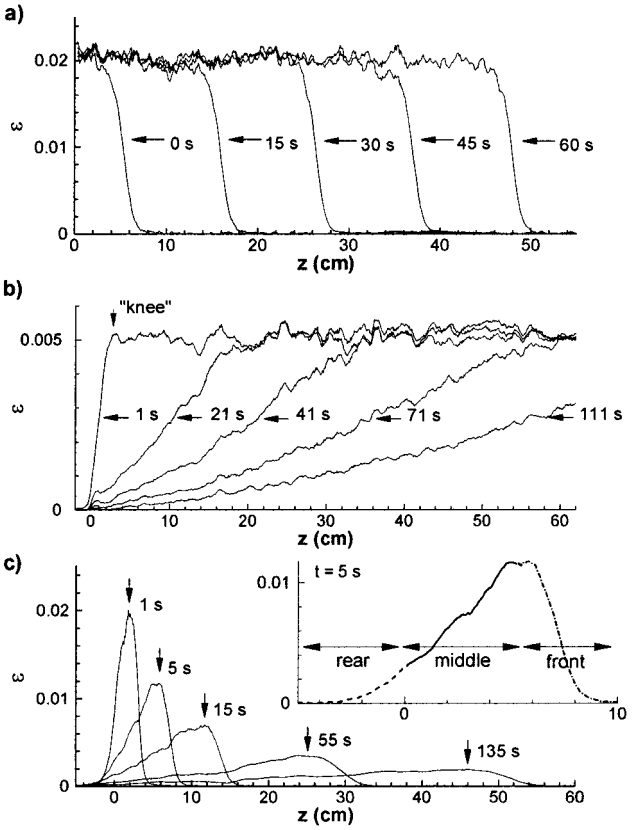

Figure 5. Profiles showing the dynamics of three foam drainage experiments: (a) *forced drainage*, (b) *free drainage*, and (c) *pulsed drainage*. Each profile is labeled by the time (in seconds) when it was taken, and the $+z$-axis is pointing in the direction of gravity. Horizontal arrows in (a) and (b) show the location of the half-maximum of the profiles. The vertical arrow in (b) shows the location of the "knee" of the pulse at $t = 1$ s. In (c) the arrows show the location of the pulse maximum for five successive profiles. All profiles have been averaged over approximately 1 cm (a few bubble diameters) and for pulsed drainage at longer times over several centimeters. The inset of (c) shows the three regions of a pulse to be discussed in section 2.5 (here for $t = 5$ s): (i) the rear, which is above the injection point (dashed line); (ii) the middle region extending from the injection point to the pulse maximum (solid line); (iii) the front, which is the region below the pulse maximum (dashed and dotted line). Note that relation (9) was used to determine ϵ.

and displayed in Figure 4, as the volume flux Φ is a controlled quantity and $v = v_f$ is directly measured without the need for an intensity calibration.

Figure 6 shows the front velocity (measured at half-maximum) versus ϵ_{main} for 15 forced drainage experiments with the flux varying over more than four decades from $\Phi = 3.0 \times 10^{-5}$ cm/s to $\Phi = 1.1$ cm/s. The error bars are determined by the standard deviations in the measured front velocity as it moves down the camera's field of view, and the relative error rapidly decreases with increasing volume fraction. The data points demonstrate a power-law dependence of v_f on ϵ_{main},

$$v_f \approx c_v \epsilon_{main}^{d_v} \qquad c_v \approx 7.94 \text{ cm/s} \qquad d_v \approx 0.60 \tag{11}$$

which is shown by the solid line.[37] The dashed line shows the expected dependence of v_f on ϵ using the traditional channel-dominated foam drainage equation based upon a rigid gas/liquid interface. Clearly, this model does not describe the data well.

Figure 7 is a log−log plot of the measured front width of the forced drainage profile against ϵ_{main}, which shows a decrease in

(37) Note that plotting v against Φ gives a power-law fit $v_f/(\text{cm/s}) = 3.66\ (\Phi/(\text{cm/s}))^{0.37}$. This is in close agreement with experiments using Dawn detergent.[5]

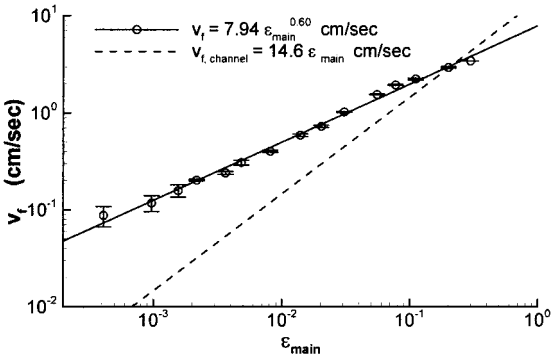

Figure 6. Front velocity v_f, plotted against main body liquid volume fraction ϵ_{main} of the forced drainage wave, determined from eq 10. The solid line is the best fit to power-law dependence (11), and the dashed line is the channel-dominated forced drainage prediction (rigid wall boundary condition).

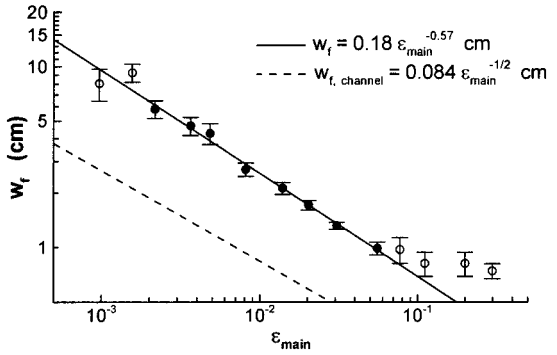

Figure 7. Forced drainage front width plotted against main body liquid volume fraction. The filled circles were used to determine the best fit power law (solid line); see eq 12. The dashed line is the prediction from channel-dominated foam drainage theory.

front width that levels off at $\epsilon \gtrsim 0.05$. The solid data points fall on a straight line, indicating power-law behavior, for which a fit yields

$$w_f \approx c_w \epsilon_{main}^{d_w} \qquad c_w \approx 0.18 \text{ cm} \qquad d_w \approx -0.57 \qquad (12)$$

The first two data points in Figure 7 ($\epsilon_{main} \lesssim 10^{-3}$) were not used for the fit, because of the extremely low signal and relatively large error in the fluorescence intensity. The dashed line shows the prediction of channel-dominated theory which captures the power-law behavior of the front width measurements for $\epsilon_{main} \lesssim 0.05$, but the prefactor is less than half that found in (12).

The leveling off of the front width can in part be attributed to the break down of the geometric approximations of section 1.1, because the assumption that the channels contain most of the liquid is no longer valid for large ϵ. Another important consideration is that our experiments study one-dimensional flow along the vertical, which is valid provided that liquid rapidly spreads horizontally as to remove radial variations in ϵ.[38] Any radial variations in the liquid volume fraction will give rise to horizontally acting capillary forces which scale as $1/R$, where $R \approx 0.63$ cm is the tube radius. The capillary force along the vertical scales inversely with the front width, $1/w_f$, and thus is weaker than the horizontal capillary force for $w_f \gtrsim R$. In this case, we expect liquid to be distributed more or less evenly throughout the cross-section of the tube, and one-dimensional flow is a good approximation. For $w_f \lesssim R$, however, capillary forces are too weak to allow for sufficient radial liquid redistribution. Instead of measuring the front of a one-dimensional wave in the vertical direction, the fluorescence intensity then picks up the radial ϵ profile. Figure 7 shows that for large $\epsilon_{main} \gtrsim 0.1$ the front width indeed saturates at $w_f \sim R$.

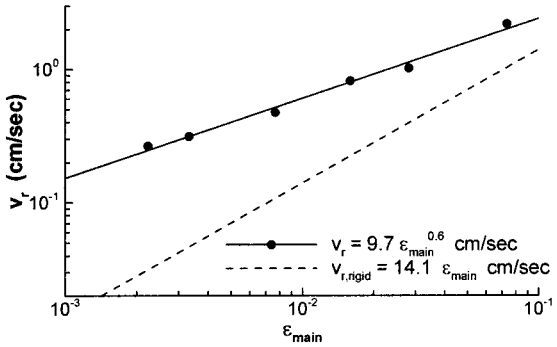

Figure 8. Rear velocity of free drainage versus main body liquid volume fraction. The solid line is the best power-law fit to the data points, and the dashed line is the channel-dominated foam drainage prediction.

2.4. Free Drainage. *Free drainage* is the evolution of the liquid volume fraction of an initially uniform foam of finite height. Figure 5b shows the experimental dynamics with initial uniform (main body) volume fraction $\epsilon_{main} \approx 5 \times 10^{-3}$. A foam of finite height is created by inserting a smaller tube into the foaming tube at the top of the camera's field of view where the injection needle is located. Sucking air through the smaller tube removes foam above the injection point. The origin of the z-axis is the location of the injection needle, which has an experimental uncertainty of about ± 1 mm and is about 5 mm (equivalent to a few bubble diameters) below the top of the foam. For the duration of the free drainage experiment, unlike the other two experiments, foaming from the bottom is halted. To achieve the initial condition of a uniform volume fraction, a continuous flux of liquid is injected, as in forced drainage, at the top of the foam, and the front is allowed to reach the bottom of the foam. At that point in time, the foam is uniform, and turning off the liquid supply marks the beginning of the free drainage experiment.

We observe that the average edge length for some free drainage experiments increased somewhat from the forced drainage value $L = 0.15 \pm 0.04$ cm. During the foaming process, the foam is pushed up through the foaming tube and there is friction of the bubbles against the walls. This friction appears to compress the bubbles inside the foaming tube. Stopping the foaming for free drainage, as well as removing foam above the injection point, relieves the compression. This increase in L induces slight changes in the prefactors c_v and c_w of (11) and (12).

Under the influence of gravity the free drainage profiles of liquid volume fraction versus height evolve such that ϵ increases monotonically from the top to the bottom of the foam at all times (see Figure 5b). Liquid continues to drain from the foam, and the profiles approach a steady state at long times.[39]

In contrast to forced drainage, where the front is moving down the foam without changing its shape, the free drainage *rear*, the region above the (uniform) main body, is getting wider with time as it moves downward. We refer to the velocity of the half-maximum point of the rear as the *rear velocity*, v_r. The solid line in Figure 8 shows the best power-law fit of v_r versus ϵ_{main}, and the dashed line shows the expected rear velocity from the channel-dominated foam drainage model.

A distinctive feature of the free drainage profiles is the "knee" (Figure 5b), which indicates the transition region between the main body and the draining foam above. The knee is measured to be moving downward at a velocity of $v_k \approx 1.5 v_r$, which will be discussed theoretically in section 4.2.2.

It is useful to track the rate at which the liquid volume fraction decreases with time. However, as is obvious from the profiles in

(38) We will show later in section 4.1 that flow through channels experiences a slipping boundary condition and is not Poiseuille-like. However, in the channels lining the foaming tube wall a no-slip boundary condition is partially imposed, which increases the viscous dissipation of these channels and decreases the liquid velocity. We thus expect in the front region that capillarity redistributes liquid from wetter channels in the center of the foaming tube to drier channels at the periphery.

(39) Princen, H. M.; Kiss, A. D. *Langmuir* **1987**, *3*, 36.

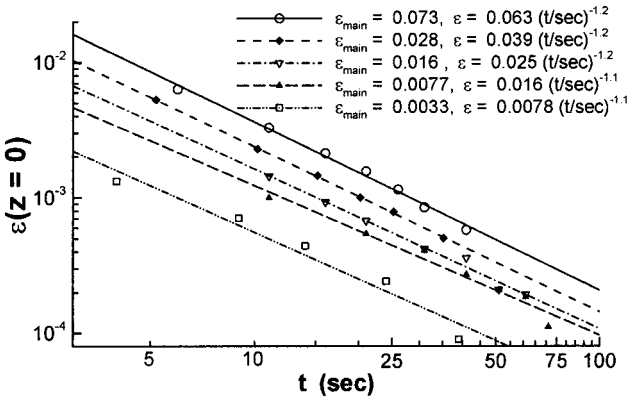

Figure 9. Decrease of liquid volume fraction at the injection point for five free drainage profiles, $\epsilon_{main} = 3.3 \times 10^{-3}$, ..., 7.3×10^{-2}. The lines show best fits to power-law behavior.

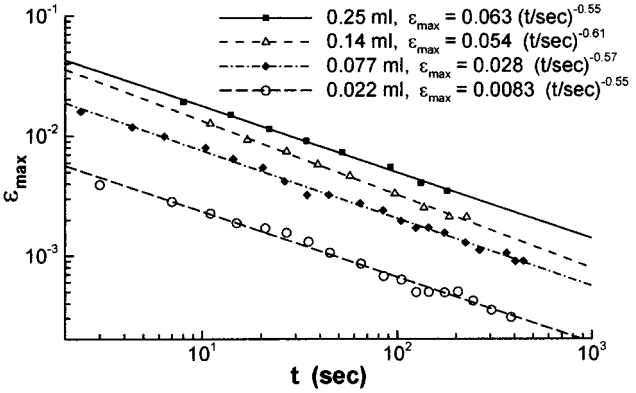

Figure 10. Peak volume fraction of the drainage pulse as a function of time for pulse volumes $V_{liq} = 0.25$, 0.14, 0.077, and 0.022 mL. Lines show best fits to power-law behavior.

Figure 5b, the dynamics depends on time and position as well. We fix the position at the injection point and plot in Figure 9 the decrease of ϵ with time for four different free drainage experiments with different main body volume fractions ϵ_{main}. Although the data cover only a small range in time, because the liquid volume fraction quickly drops to immeasurably small values, it appears that there is a rough power-law dependence with $\epsilon \propto t^{-1.2}$. We point out that the channel-dominated drainage equation applied to free drainage[40] predicts that $\epsilon \propto t^{-2/3}$ for points close to the top of the foam.

2.5. Pulsed Drainage. *Pulsed drainage* is the evolution of a (small) finite volume of liquid ("pulse") injected into a foam with very low liquid content; the injected volume has an uncertainty of ±0.005 mL. As with free drainage, the position of the injection needle marks the origin for the *z*-axis. The bolus is injected within 1 s using the syringe pump, and the end of the injection sets the time $t = 0$, which is known within ±1 s. Gravity pulls the injected liquid downward, and capillarity spreads the pulse in all directions, as shown by the liquid volume fraction profiles in Figure 5c. Convenient reference points of the profiles are the peak height (maximum liquid volume fraction) ϵ_{max} and peak position z_{max} of the pulse.

Data for the decrease of ϵ_{max} with time from four experiments with different injection volumes are shown in Figure 10. Figure 11 shows the corresponding motion of z_{max} in time. Both figures span one decade in pulse volume and several decades in time. The larger pulses travel downward faster and by $t \approx 200$ s have moved outside the field of view, which ends at $z \approx 70$ cm. The two smaller pulses stay in the field of view longer; however, their fluorescence signals are much weaker.

(40) Koehler, S. A.; Stone, H. A.; Brenner, M. P.; Eggers, J. *Phys. Rev. E* **1998**, *58*, 2097.

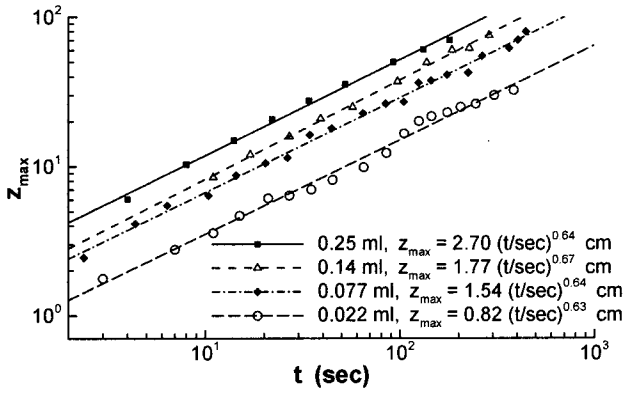

Figure 11. Peak position of the drainage pulse as a function of time for pulse volumes $V_{liq} = 0.25$, 0.14, 0.077, and 0.022 mL. Lines show best fits to power-law behavior.

The data points fall on straight lines on the log−log plot, and power-law behaviors

$$\epsilon_{max} = c_\epsilon t^{d_\epsilon} \qquad z_{max} = c_z t^{d_z} \tag{13}$$

are observed, with $d_\epsilon \approx -0.57$ and $d_z \approx 0.65$. Again we observe (small) deviations from the channel-dominated foam drainage theory, which predicts $d_\epsilon = -1/2$ and $d_z = +1/2$.[40]

We verified that the total liquid content, which is determined from the integral under the ϵ-profiles (cf. Figure 5c), is conserved provided that the complete pulse remains within the field of view of the camera. This also supports the validity of our intensity calibration.

3. Energy Argument for the Foam Permeability

As discussed in section 1.2, our task will be the derivation of a generalized foam permeability $k(\epsilon)$ which accounts for the viscous dissipation in *both* channels and nodes.

In order to derive $k(\epsilon)$, we consider the energy balance over a "dog-bone" foam network unit (Figure 1c) with liquid volume ν. All dissipation in the gas bubbles is neglected, and we only consider dissipation in the liquid. If one balances the rate of work per unit volume of foam done by pressure and body forces against the rate of work done by viscous stresses, one obtains (from the Stokes equation)

$$\int_\nu \mathbf{u}_m \cdot (\rho \mathbf{g} - \nabla_m p_m)\, \mathrm{d}\nu = -\int_\nu \mu \mathbf{u}_m \cdot \nabla_m^2 \mathbf{u}_m\, \mathrm{d}\nu \tag{14}$$

where $\rho\mathbf{g}$ is the gravitational force and p_m and $\mathbf{u}_m$ are the microscopic pressure and velocity field, respectively. The rate of work per unit volume that drives the flow in the network unit (left-hand side of (14)) can be rewritten as

$$\mathbf{u} \cdot \mathbf{G} \nu \tag{15}$$

where $\mathbf{G} = \rho\mathbf{g} - \nabla p$ is the macroscopic driving pressure gradient (3). By dropping the subscript m, we indicate that averages over the network unit have been performed, making the resulting quantities macroscopic. The liquid volume ν consists of two quarter-node contributions $\nu_n \approx \delta_n r^3/2$ and a channel contribution $\nu_c \approx \delta_\epsilon r^2 L$; see discussion after (2). Removing length and velocity scales from inside the integral on the right-hand side of (14) yields

$$\mu u^2 \left(\frac{\delta_n r}{2} \int_{2\nu_n/\delta_n r^3} \left(\frac{\mathbf{u}_m}{u}\right) \cdot r^2 \nabla_m^2 \left(\frac{\mathbf{u}_m}{u}\right) \frac{2\mathrm{d}\nu}{\delta_n r^3} + \delta_a L \int_{\nu_c/\delta_a r^2 L} \left(\frac{\mathbf{u}_m}{u}\right) \cdot r^2 \nabla_{\perp m}^2 \left(\frac{\mathbf{u}_m}{u}\right) \frac{\mathrm{d}\nu}{\delta_a r^2 L} + \frac{\delta_a r^2}{L} \int_{\nu_c/\delta_a r^2 L} \left(\frac{\mathbf{u}_m}{u}\right) \cdot L^2 \nabla_{\parallel m}^2 \left(\frac{\mathbf{u}_m}{u}\right) \frac{\mathrm{d}\nu}{\delta_a r^2 L} \right) \tag{16}$$

where $\nabla^2_{||m}$ is the longitudinal component of the Laplacian along the channel, which has a typical scale of L^{-2}, and $\nabla^2_{\perp m}$ is its transverse component with scale r^{-2}. We have indicated explicitly the scales of terms in order to characterize the relative sizes of the sources of dissipation. The first term in (16) is the rate of viscous dissipative work of the flow in the two node regions, while the second and third are respectively the rate of transverse and (extensional and compressional) longitudinal dissipative work in the channel.

Combining (14)−(16) yields

$$\mathbf{G}\cdot\hat{\mathbf{u}} \approx -\mu u\left(\frac{\delta_n}{2\delta_a rL}\int_{\tilde{v}_n}\tilde{\mathbf{u}}_m\cdot\tilde{\nabla}^2_m\tilde{\mathbf{u}}_m\,d\tilde{v} + \frac{1}{r^2}\int_{\tilde{v}_c}\tilde{\mathbf{u}}_m\cdot\tilde{\nabla}^2_{\perp m}\tilde{\mathbf{u}}_m\,d\tilde{v} + \frac{1}{L^2}\int_{\tilde{v}_c}\tilde{\mathbf{u}}_m\cdot\tilde{\nabla}^2_{||m}\tilde{\mathbf{u}}_m\,d\tilde{v}\right) \quad (17)$$

where ˜ denotes dimensionless quantities and $\hat{\mathbf{u}}$ is the unit vector in the direction of flow in the dog-bone network unit. v in (15) has been approximated by $v_c \approx \delta_a r^2 L$, consistent with the small liquid volume fraction limit and the approximations that lead to (2).

A foam is composed of many such interconnected network units with different orientational angles θ between the axis of the unit channel $\hat{\mathbf{u}}$ and the direction of the driving pressure gradient $\hat{\mathbf{G}}$. The average liquid velocity of a region of foam is then given by the average $\mathbf{v}\equiv\langle\mathbf{u}\rangle_\theta$ over all orientations. Averaging (17) over all angles gives

$$\frac{\mathbf{G}}{3} \approx -\mu\mathbf{v}\left(\frac{\delta_n}{2\delta_a rL}\int_{\tilde{v}_n}\tilde{\mathbf{u}}_m\cdot\tilde{\nabla}^2_m\tilde{\mathbf{u}}_m\,d\tilde{v} + \frac{1}{r^2}\int_{\tilde{v}_c}\tilde{\mathbf{u}}_m\cdot\tilde{\nabla}^2_{\perp m}\tilde{\mathbf{u}}_m\,d\tilde{v} + \frac{1}{L^2}\int_{\tilde{v}_c}\tilde{\mathbf{u}}_m\cdot\tilde{\nabla}^2_{||m}\tilde{\mathbf{u}}_m\,d\tilde{v}\right) \quad (18)$$

As expected the average flow velocity is along $\mathbf{G}$. The factor of 3 results from the angular average $\langle\mathbf{G}\cdot\hat{\mathbf{u}}\rangle_\theta = G\int_0^1\cos^2(\theta)\,d\cos(\theta) = G/3$.

Thus we have successfully made the transition from a microscopic equation like (14) to a formula on macroscopic scales equivalent to Darcy's law, (3). If one compares (3) and (18), the effective permeability of the foam is

$$k(\epsilon) \approx \left(\frac{3\delta_n}{2\delta_a rL}I_n + \frac{3}{r^2}I_{c\perp} + \frac{3}{L^2}I_{c||}\right)^{-1} \approx \left(\frac{\delta_n\delta_\epsilon^{1/2}}{2\delta_a\epsilon^{1/2}}I_n + \frac{\delta_\epsilon}{\epsilon}I_{c\perp} + I_{c||}\right)^{-1}\frac{L^2}{3} \quad (19)$$

where I_n, $I_{c\perp}$, and $I_{c||}$ have been introduced as abbreviations for the absolute values of the corresponding dimensionless dissipative work integrals in (18). The second approximation in (19) uses $r(\epsilon)$ from (2) to arrive at an expression for $k(\epsilon)$. An explicit calculation of these dimensionless integrals in general is quite difficult, and beyond the scope of this work, except for the simple case of no-slip channel walls (i.e. Poiseuille-like flow) as we discuss in the next section. Nonetheless we will treat I_n, $I_{c\perp}$, and $I_{c||}$ as dimensionless numbers that for a given foam are independent of ϵ and L.

3.1. Boundary Conditions. The relative contribution of each of the three terms in eq 19 to the permeability of a foam is influenced by the relative liquid volume in the channels and nodes and also is crucially dependent on the boundary conditions at the gas/liquid interface which affect the dimensionless integrals I_n, $I_{c\perp}$, and $I_{c||}$.

The original foam drainage model[19,23] is based upon a no-slip (i.e. zero-velocity) boundary condition, making the flow in the channels Poiseuille-like. The second term of (19) then makes the dominant contribution to $k(\epsilon)$ because $r \ll L$, and the permeability is

$$k(\epsilon) = K_1 L^2\epsilon \quad K_1 \equiv (3\delta_\epsilon I_{c\perp})^{-1} \quad (20)$$

From numerical calculations for flow through a rigid, straight channel with a scalloped-triangle cross section (see Figure 1b) it follows that[5,7] $K_1 \approx 6.3\times10^{-3}$. Equation 20 is indeed the proportionality $k(\epsilon)\propto\epsilon$ inferred from the physical argument discussed in section 1.3. As the dissipation in the nodes is negligible here, we call the foam drainage equation resulting from (7) and (20) *channel-dominated*. In its one-dimensional form, (7) for rigid gas/liquid interfaces can be written as

$$\mu\frac{\partial\epsilon}{\partial t} + K_1\rho g L^2\frac{\partial\epsilon^2}{\partial z} - \frac{\gamma\delta_\epsilon^{1/2}K_1 L}{3}\frac{\partial^2\epsilon^{3/2}}{\partial z^2} = 0 \quad (21)$$

where the $+z$ axis points along the direction of gravity.

Two arguments have been made to support the no-slip boundary condition. The first is based upon the assumption that the liquid in the faces is essentially stationary. Any motion of the channel walls results in a surface shear against the rigid faces, which is resisted by the surface viscosity. If the surface (shear) viscosity is large, the surface mobility is low, and the channel boundaries are approximately rigid. Kraynik[4] proposed that the surface shear viscosity μ_s should fulfill $\mu_s \gtrsim 10r\mu$ in order to justify the assumption of rigid walls. The surface viscosity is highly dependent on the surfactant species and concentration, and unfortunately, there is considerable uncertainty in the measured values of μ_s even for well-defined surfactant systems such as aqueous solutions of SDS.[41] The range of typical values $\mu_s \sim 10^{-4}-10^{-2}$ g/s [42] allows for violations of the "Kraynik criterion" for large enough r.

A second argument in favor of a no-slip interface is that the liquid flow through the channels will shear surfactants off the top portion of the channel surface and push them toward the bottom of the channel. If the diffusion and adsorption times for surfactants in the bulk to replenish the surfaces are large, then a surfactant concentration gradient in the direction of the downward flow is created. This sets up a surface (Marangoni) stress that will oppose the downward flow of the surface and so reduce the surface velocity. Again, it is difficult to assess a priori the time scales of exchange of surfactant between surface and bulk.

An alternative physical limit to consider is the case of very small surface stresses,[5] which should be valid for low surface viscosities, mobile faces, and small surfactant concentration gradients along the surface. We remind the reader that the injected liquid in our experiments is the same soap solution used to generate the foam, so that the injection will not automatically set up any surface stresses. If, in addition, the surfactant molecules adsorb and desorb from the surface quickly enough to equilibrate on the time scales of the flow, surfactant concentration gradients should be small and the surfaces would be nearly stress-free. Indeed, when comparing low molecular weight

(41) Buzza, D. M. A.; Lu, C.-Y. D.; Cates, M. E. *J. Phys. II* **1995**, *5*, 37−52.

(42) Shah, D. O.; Djabbarah, N. F.; Wasan, D. T. *Colloid Polym. Sci.* **1978**, *256*, 1002.

surfactants such as SDS to surface active proteins, Wilde et al.[22] describe the interfaces of the former as highly mobile.

In the case of mobile interfaces, the flow in the channels is pluglike with some degree of extension/compression toward the top and bottom ends of the channel where the cross-sectional area varies (see Figure 1b,c). Thus, in contrast to the rigid-wall case, $I_{c\perp}$ is not necessarily the dominant term. However, even for a stress-free wall with perfect slip, there will be dissipation in the nodes due to the merging, mixing, and bending of the flow (see the Introduction and Figure 1b; laminar viscous flow in curved channels is referred to as Dean flow[43]). The first term of (19) will then dominate (the third term is negligible because $L \gg r$, as before), and the permeability becomes

$$k(\epsilon) = K_{1/2} L^2 \epsilon^{1/2} \qquad K_{1/2} \equiv \frac{2\delta_a}{3\delta_\epsilon^{1/2}\delta_n I_n} \tag{22}$$

which is in agreement with the force balance in section 1.3. The permeability coefficient $K_{1/2}$ is determined by the geometry of the node walls and the flow field inside the nodes.[44] We have to caution, though, that experiments varying bubble size suggest a slight dependence of $K_{1/2}$ on L not explicitly indicated in (22). We believe this weak L-dependence may arise either from interfacial rheology or from bubble deformations due to hydrostatic pressure variations. We are not aware of any calculation of the dimensionless dissipation integral I_n; however an experimentally deduced value is reported in section 4.1. Because of the dominance of node dissipation we call the equation obtained from (7) with the foam permeability (22) the *node-dominated foam drainage equation*

$$\mu\frac{\partial\epsilon}{\partial t} + K_{1/2}\rho g L^2 \frac{\partial\epsilon^{3/2}}{\partial z} - \frac{K_{1/2}\delta_\epsilon^{1/2} L\gamma}{2}\frac{\partial^2\epsilon}{\partial z^2} = 0 \tag{23}$$

given here in its one-dimensional form projected onto the z-axis. Note that the exponents in (23) differ from those in (21) which is due to the change in the permeability's dependence on ϵ (cf. (20) and (22)).

The approach assuming moving, stress-free walls does not seem unrealistic considering that it has been known for some time that the gas/liquid interfaces in a foam do not have to be rigid. In experiments involving soap films, observers have distinguished between rigid and (simple or irregular) mobile films.[13] In our foam system we visually observe motion in the faces, similar to that described by Leonard and Lemlich.[7]

4. Analysis and Comparison to Experiment

Armed with a generalized theory for foam permeability (section 3) and data from three types of experiments (section 2), we now proceed to discuss the dynamics of foam drainage in more detail. We begin with forced drainage and show that our data supports the node-dominated model. In subsequent sections we use the node-dominated equation (23) to analyze and elucidate the experimental results for free and pulsed drainage from sections 2.4 and 2.5. The dynamics of the channel-dominated theory has been described in a previous publication.[40]

4.1. Forced Drainage. The natural decomposition of the traveling wave profile into a well-drained region, front region, and main body region (cf. section 2.3 and Figure 5a) sets three characteristic scales for a particular experiment: (i) a length scale, proportional to the front width w_f, (ii) a velocity scale proportional to the front speed v_f, and (iii) the liquid volume fraction of the main body, ϵ_{main}. These characteristic scales are determined by physical parameters, such as surface tension, density, gravitational acceleration, and viscosity as well as experimental parameters such as liquid flux and bubble size. We will later use these scales to normalize experimental data as well as computational results.

To arrive at a theoretical description of forced drainage, we make the following ansatz for a traveling volume fraction profile, $\epsilon(z, t) = \epsilon(s \equiv z - v_f t)$; i.e., we transform into a frame of reference moving with the drainage wave speed v_f. Using this ansatz in the generalized foam drainage equation (7), integrating once with respect to s and using the boundary condition $\epsilon(\infty) = 0$ yields

$$-\mu v_f + k(\epsilon)\left(\rho g - \frac{\delta_\epsilon^{1/2}\gamma\,\mathrm{d}\epsilon}{2L\epsilon^{3/2}\mathrm{d}s}\right) = 0 \tag{24}$$

In the main body region of the wave above the front, the liquid volume fraction is constant, $\epsilon(-\infty) = \epsilon_{main}$. The ϵ-derivative in (24) then vanishes, and a simple relationship between permeability and volume fraction results,

$$k(\epsilon_{main}) = \frac{\mu v_f}{\rho g} \approx \frac{\mu c_v}{\rho g}\epsilon_{main}^{d_v} \tag{25}$$

where the second equality follows from the experimentally observed power-law behavior (11). Comparison of the measured $d_v \approx 0.6$ with the channel-dominated (i.e. "no-slip") approximation (20), $k(\epsilon) \propto \epsilon$, and the node-dominated (i.e. "no-stress") approximation (22), $k(\epsilon) \propto \epsilon^{1/2}$, shows that the permeability is closer to being dominated by the nodes, at least for the aqueous foams used here. In particular, from (22) and (25) the model predicts that the forced drainage velocity is

$$v_f = V_F \epsilon_{main}^{1/2} \qquad V_F = K_{1/2}\rho g L^2/\mu \tag{26}$$

with $K_{1/2}$ defined in (22). Since we are unable to compute $K_{1/2}$, we determine it from the experimental data for v_f (Figure 6). In order to obtain a controlled comparison to node-dominated theory, however, we must not use the original fit (11) with $d_v \approx 0.60$, but instead perform a best fit of the measured data to (26), where $d_v = 1/2$ exactly. The result is

$$v_f \approx \tilde{c}_v \epsilon_{main}^{1/2} \qquad \tilde{c}_v \approx 5.12\ \mathrm{cm/s} \tag{27}$$

which, by comparison to (26), identifies the theoretical velocity scale V_F with the measured $\tilde{c}_v$. With $\rho = 1\ \mathrm{g\ cm^{-3}}$, $g = 981\ \mathrm{cm\ s^{-2}}$, $\mu = 0.01\ \mathrm{g\ cm^{-1}}$, and $L = 0.15$ cm, we obtain[45] $K_{1/2} \approx 2.3 \times 10^{-3}$. Using eq 22 and approximating[28] $\delta_n \approx 0.3$ gives $I_n \approx 400$ for the dimensionless node

(43) Leal, G. *Laminar Flow and Convective Transport Processes*; Butterworth-Heinemann: Boston, MA, 1992.

(44) The convention we adopt for the subscript of the permeability coefficient is $k(\epsilon) = K_\chi L^2 \epsilon^\chi$; $\chi = 1/2$ for node-dominated drainage, and $\chi = 1$ for channel-dominated drainage.

(45) It is instructive to consider the permeability of an fcc-close-packed bed of spheres ($\epsilon_{fcc} \approx 0.26$), which has the same geometry as a monodisperse foam at the critical volume fraction $\epsilon = \epsilon_{fcc}$ composed of spherical bubbles. In our notation, $k_{fcc} \approx (2a^2)/(9(1 - \epsilon_{fcc})435)$ for spheres of radius a.[30] The equivalent sphere radius for the foam follows from the volume of a cell ($2^{7/2}L^3 = 4\pi a^3/3$) to be $a \approx 1.4L$. Substituting for a yields $k_{fcc} \approx 1.4 \times 10^{-3} L^2$. Similar permeabilities are predicted by both foam drainage models: the node-dominated model (mobile gas/liquid interfaces) predicts $k(\epsilon_{fcc}) \approx 1.2 \times 10^{-3} L^2$, and the channel-dominated model (rigid gas/liquid interface) yields $k(\epsilon_{fcc}) \approx 1.6 \times 10^{-3} L^2$. Although both foam drainage models are strictly valid for dry foams only (i.e. $\epsilon \ll \epsilon_{fcc}$), this calculation shows that the modeled permeability is still reasonable even in the limit of wet foams.

dissipation integral in (19), compared with $I_{c\perp} \approx 310$ for the channel-dominated theory.

Is node-dominated drainage a valid description for all of our different types of experiments? Much work has been devoted to the channel-dominated foam drainage model with rigid walls.[8,40] We will focus in the present work on the other limit of plug-flow in the channels and dissipation in the nodes. Although the data for the foam we study here do not exactly match the predictions of either limit, we will show in the remainder of the paper that the agreement with the node-dominated model of foam drainage is much better.

We continue our analysis of the node-dominated model by shifting our focus from the uniform main body to the front region of the forced drainage wave. In the front region ϵ decreases from ϵ_{main} to 0, so that the derivative (capillary) term of (24) becomes important. Using (22), (24), and (26) yields a nonlinear ODE for $\epsilon(s)$,

$$\frac{d\epsilon}{ds} = \frac{2L\rho g}{\delta_\epsilon^{1/2}\gamma}(\epsilon^{3/2} - \epsilon_{main}^{1/2}\epsilon) \qquad (28)$$

A characteristic (capillary) length scale for a foam is

$$Z_F = \frac{\delta_\epsilon^{1/2}\gamma}{2L\rho g} \qquad (29)$$

Defining the new variables $\tilde{s} = s\epsilon_{main}^{1/2}/Z_F$ and $\tilde{\epsilon} = \epsilon/\epsilon_{main}$ reduces (28) to

$$d\tilde{\epsilon}/d\tilde{s} = \tilde{\epsilon}^{3/2} - \tilde{\epsilon} \qquad (30)$$

Imposing the boundary condition $\tilde{\epsilon}(-\infty) = 1$ leads to the solution

$$\tilde{\epsilon}(\tilde{s}) = (1 + e^{\tilde{s}/2})^{-2} \qquad (31)$$

which is formally the square of a Fermi function. This shows analytically that the node-dominated foam drainage equation (as well as the channel-dominated one[8]) admits a solitary wave solution with unchanging wave profile. This should not be too surprising considering the similarity of equations like (21) and (23) with the Burgers equation and other well-known PDEs with soliton solutions.[46]

The dimensionless width of the front region Δ_s is defined as the distance between the points in the profile where $\tilde{\epsilon} = 0.8$ and $\tilde{\epsilon} = 0.2$, to match the experimental criterion (see section 2.3). Using (31), we find $\Delta_s \approx 4.7$, making the dimensional front width

$$w_f = \Delta_s Z_F \epsilon_{main}^{-1/2} = \frac{\Delta_s \delta_\epsilon^{1/2}\gamma}{2L\rho g}\epsilon_{main}^{-1/2} \qquad (32)$$

We note that any equation based upon (1) and (7) predicts that the front width will scale with $\epsilon_{main}^{-1/2}$. The measured front width exponent $d_w \approx -0.57$ is in fairly close agreement. A ring-tensiometer measurement gives $\gamma \approx 32$ dyne/cm[47] and substituting into (32) predicts a front width prefactor $c_w \approx 0.21$ cm. For consistent comparison to experiment, we again replace our best fit (12) by a fit with the theoretical exponent $d_w = -1/2$ and find

$$w_f \approx \tilde{c}_w \epsilon_{main}^{-1/2} \qquad \tilde{c}_w \approx 0.256 \text{ cm} \qquad (33)$$

The best-fit prefactor, $\tilde{c}_w$, is much closer to the node-dominated prediction than to the channel-dominated prediction of 0.084 cm. This fit also provides us with an experimental value for the length scale Z_F, as $Z_F = \tilde{c}_w/\Delta_s \approx 0.0545$ cm.

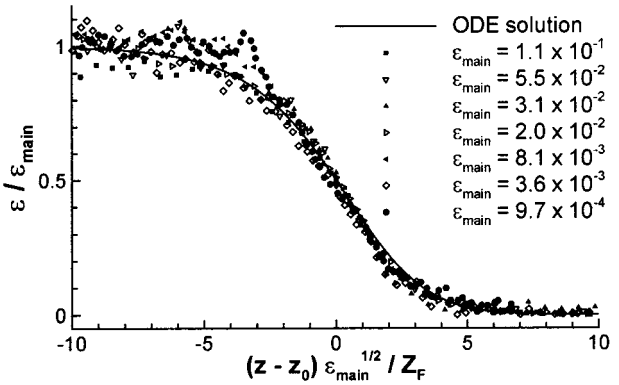

Figure 12. Collapse of the front profiles of forced drainage waves for seven different volume fractions ϵ_{main} (symbols) onto a universal curve. The solid line is the analytical result of (31) which predicts the shape of the wave profile from the node-dominated foam drainage eq 23. The curves have been aligned such that the coordinate $z - z_0 = 0$ coincides with the center of the front region, where we select a value z_0 for each data set.

The analytical solution (31) can be compared with the complete measured profile of the wave front at various ϵ_{main} by rescaling using Z_F and ϵ_{main}. Figure 12 shows that all data collapse onto a universal curve, in excellent agreement with the theoretical prediction. Thus, all the spatial and temporal characteristics of forced foam drainage are captured accurately within the node-dominated model.

4.2. Free Drainage. Though the free drainage experiment is conceptually simple, a theoretical description of this process is considerably more involved than for forced drainage. This is largely due to the more complicated boundary conditions for ϵ, namely, zero flux at the top of the foam and $\epsilon = \epsilon_{crit}$ at the bottom, where the foam is in contact with the soap solution and the bubbles are spherical. The latter condition uses the *critical* volume fraction ϵ_{crit}, which corresponds to the void fraction of close packing of spherical bubbles. In our experiments, the bottom boundary is far below the field of view of the camera, so that we do not have to deal with it explicitly.

It is convenient to divide a free-draining foam into two overlapping regions that grow with time: the rear region which contains the top of the foam and the knee region where the liquid volume fraction plateaus to ϵ_{main} (cf. section 2.4). The knee is moving downward with a constant velocity v_k, which experiments show to be greater than the front velocity of forced drainage v_f for the same ϵ_{main}. It is also greater than the rear velocity v_r, so that the rear region grows over time (see Figure 5b).

4.2.1. Rear Region. At time $t = 0$, a uniform profile $\epsilon(z, 0) = \epsilon_{main}$ has been established, and the flux of liquid injected into the foam at $z = 0$ is turned off. The no-flux top boundary condition requires that the liquid velocity $v = 0$ at $z = 0$ for $t > 0$ (otherwise the foam would be shrinking in height). For node-dominated drainage this yields

$$\rho g \epsilon^{3/2} - \frac{\delta_\epsilon^{1/2}\gamma}{2L}\frac{\partial \epsilon}{\partial z} = 0 \qquad (z = 0) \qquad (34)$$

which follows from (3), (5), and (22).

(46) Grundy, R. E. *IMA J. Appl. Math.* **1983**, *31*, 121−137.

(47) A common value reported in the literature for the surface tension of SDS is 30 dyne/cm.[36]

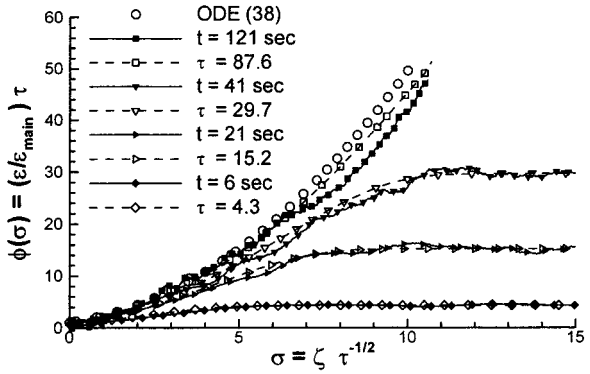

Figure 13. Rear region of simulated and experimental free drainage profiles in rescaled dimensionless coordinates for successive times, starting with a uniform profile. Filled-in symbols are measurements for $\epsilon_{main} \approx 0.0077$, rescaled using a forced drainage experiment, as explained in the text. All open symbols are simulations: the open circles show the ODE solution (38), and symbols connected by dashed lines are simulations of the full PDE (36) with the no-flux top boundary condition (34). The dimensionless times τ correspond to the measured times t for the experimental profiles. For long times the profiles collapse onto the ODE solution (38).

We define characteristic time and length scales

$$T_F = \frac{\delta_\epsilon^{1/2}\gamma\mu}{2K_{1/2}(\rho g)^2 L^3} \qquad Z_F = \frac{\delta_\epsilon^{1/2}\gamma}{2\rho g L} \tag{35}$$

which are the same as in the forced drainage problem discussed before (see section 4.1); i.e., $T_F = Z_F/V_F = \tilde{c}_w/(\Delta_s \tilde{c}_v) \approx 0.0106$ s. To nondimensionalize the node-dominated foam drainage equation (23), we transform variables according to $\tilde{\epsilon} = \epsilon/\epsilon_{main}$, $\zeta = z\epsilon_{main}^{1/2}/Z_F$, and $\tau = t\epsilon_{main}/T_F$ and arrive at the dimensionless foam drainage equation

$$\frac{\partial\tilde{\epsilon}}{\partial\tau} + \frac{\partial\tilde{\epsilon}^{3/2}}{\partial\zeta} - \frac{\partial^2\tilde{\epsilon}}{\partial\zeta^2} = 0 \tag{36}$$

In order to solve (36) numerically, we have to impose a second boundary condition on ϵ in addition to (34). Here we are only interested in the top region of the profile far above the foam/liquid interface, so we impose $\tilde{\epsilon}(\infty, t) = 1$ at the bottom of our simulation. Using the IMSL routine DMOLCH we obtain the drainage profiles shown in Figure 13 by the connected open symbols. We have plotted the results in rescaled coordinates, because we can obtain a self-similar solution in this coordinate system as well. In the spirit of our previous work,[40] we note that a transformation of variables according to

$$\tilde{\epsilon} = \tau^{-1}\,\phi(\sigma) \qquad \sigma = \zeta\tau^{-1/2} \tag{37}$$

balances all the terms in (36). This leads to self-similar solutions $\phi(\sigma)$ obeying the ordinary differential equation

$$-\phi - \frac{1}{2}\sigma\phi' + (\phi^{3/2} - \phi')' = 0 \tag{38}$$

with $'$ denoting differentiation with respect to σ. The leading-order solution of (38) is

$$\phi(\sigma) \approx (2\sigma/3)^2 \qquad (\sigma \gg 1) \tag{39}$$

which is valid for $\sigma \le 3\tau^{1/2}/2$ (otherwise $\tilde{\epsilon} > 1$). The top no-flux boundary condition (34) transforms into

$$\phi^{3/2} - \phi' = 0 \qquad (\sigma = 0) \tag{40}$$

To solve the ODE (38), we use a shooting algorithm to ensure that the solution asymptotes to the parabolic approximation (39) for the largest $\sigma = \sigma_{max}$ of the integration range (typically, $\sigma_{max} \sim 10$). The resulting solution is plotted as open circles in Figure 13. It is approached by the solution of the full PDE at large τ. At any given finite time, however, the rescaled profile reaches its maximum at the knee (to be discussed in the next section) and plateaus at a value of $\phi = \tau$.

The parabolic approximation (39) can be rewritten in $(\tilde{\epsilon}, \zeta, \tau)$ space as

$$\tilde{\epsilon} \approx (2\zeta/3\tau)^2 \tag{41}$$

Note that only for very long times are (39) and (41) good approximations, because only then is their range of validity $(\tau^{1/2} \ll \zeta < 3\tau/2)$ appreciable.

Figure 13 also shows rescaled experimental data (filled symbols) in the self-similar coordinates $\tilde{\epsilon}\tau$ versus $\zeta\tau^{-1/2}$. The length and time scales are determined from the forced drainage experiment with the same ϵ_{main}, as discussed in the previous section. The rescaled experimental data are in very good agreement with the simulations at the corresponding dimensionless times. This figure shows that the rear portion of the experimental profile is indeed parabolic in rescaled coordinates (see eq 39) and not linear, $\epsilon \approx \zeta/2\tau$, as predicted by the channel-dominated foam drainage equation.[40]

Next, we return to the issue raised in section 2.4 pertaining to Figure 8, which shows that the measured rear velocity is considerably higher than that predicted by the channel-dominated model. From eq 41 it is easy to see that the half-maximum at the rear is at a position ζ given by

$$\left(\frac{2\zeta}{3\tau}\right)^2 = \frac{1}{2} \Rightarrow \zeta = \frac{3\tau}{2^{3/2}} \tag{42}$$

It follows that the predicted rear velocity $v_r = (3/2^{3/2})V_F\epsilon_{main}^{1/2} \approx 1.06\ V_F$. The measured rear velocity of free drainage can be fitted to the node-dominated formula to yield $v_r \approx 6.13\ \epsilon_{main}^{1/2}$ cm/s, which is in fairly good agreement with the prediction above using $V_F = \tilde{c}_v$; see (27). The predicted rear velocity is about 10% below measurements, which can be attributed to the slightly larger bubbles of the free drainage experiment as described in section 2.4.

Figure 9 previously illustrated that at a fixed position in space near the top of the foam free drainage proceeds as $\epsilon \propto t^{-1.2}$ and not $\epsilon \propto t^{-2/3}$ as predicted by the channel-dominated model.[40] However, this measurement is consistent with the node-dominated foam drainage equation. Close to the top, for $\sigma = \zeta\tau^{-1/2} \ll 1$, it follows from (37) that $\tilde{\epsilon} \approx \tau^{-1}\phi(0)$. For long enough times, then, $\tilde{\epsilon} \propto \tau^{-1}$ is valid for a considerable range of ζ values. Note that the initial decrease in volume fraction is faster, as for times $\tau^{1/2} \ll \zeta$ the parabolic approximation (41) holds, and $\tilde{\epsilon} \propto \tau^{-2}$.

4.2.2. The "Knee". The main body of the drainage profile with uniform $\epsilon = \epsilon_{main}$ begins at the knee, which is moving downward in time. Using similar arguments as for the rear velocity (42), we expect the center of the knee (intersection of the rear and main body regions) to be at $\zeta = 3\tau/2$ in dimensionless coordinates. This means that the knee velocity v_k is predicted to be $v_k = \sqrt{2}v_r$ (cf. (42)), which agrees well with the measured v_r (section 2.4). In

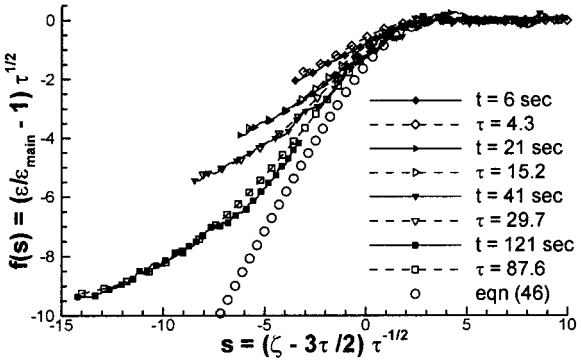

Figure 14. Free drainage profiles in the transition region (about the "knee") for experiment and simulation at successive times in rescaled (f, s) coordinates; see (43). Filled-in symbols are measurements for $\epsilon_{main} \approx 0.0077$, rescaled according to the preceding forced drainage experiments that create uniform profiles, as described in the text. All open symbols are simulations: the open circles show the ODE solution (46), and connected symbols show simulations of the full PDE (36) with the no-flux top boundary condition (34), at times τ corresponding to experiment.

contrast the channel-dominated foam drainage theory predicts that the knee velocity is *twice* the rear velocity.

For $\zeta \gg 3\tau/2$, $\tilde{\epsilon}$ should saturate to 1, and so we seek a self-similar solution to the dynamics in the transition region about $\zeta \sim 3\tau/2$ of the form

$$\tilde{\epsilon} = 1 + \tau^{-1/2} f(s) \qquad s \equiv (\zeta - 3\tau/2)\tau^{-1/2} \tag{43}$$

Inserting (43) into (36) and expanding $\tilde{\epsilon}^{3/2}$ up to second order in $\tau^{-1/2} f(s)$, we obtain

$$f + sf' + \left(-\frac{3}{4}f^2 + 2f'\right)' + O(\tau^{-1/2}) = 0 \tag{44}$$

In the long-time limit, the error to this approximation becomes vanishingly small. Collapsing the numerical simulations of the PDE in this fashion validates the ansatz, as shown in Figure 14. Integrating (44) once gives

$$sf - \frac{3}{4}f^2 + 2f' = 0 \tag{45}$$

where the integration constant is set to zero because $f(+\infty) = 0$. The solution to (45) is

$$f(s) = -\frac{8e^{-s^2/4}}{3\pi^{1/2}\,\mathrm{erf}(s/2) + C} \tag{46}$$

The constant C should be chosen to match (46) onto the parabolic approximation, $\tilde{\epsilon} \approx (2\zeta/3\tau)^2$ from eq 39. To leading order this requires $f(s) \to -4s/3$ for $s \to -\infty$. From (37) and (43) one obtains $s = \sigma - 3\tau^{1/2}/2$, so that at large enough τ the conditions $\sigma \gg 1$ and $s \ll -1$ can indeed be fulfilled simultaneously. Thus, we find $C = 3\sqrt{\pi}$, and the corresponding solution (46) is plotted as open circles in Figure 14. Again, the solutions of the PDE (36) approach the self-similar solution in rescaled (f,s) coordinates for long times; see Figure 14.

We repeat this rescaling for our experimental data as shown by the solid symbols in Figure 14. As in the previous section, the profiles agree very well with theory. The small mismatches between the simulated and measured profiles can be attributed to uncertainties in the characteristic time and length scales. For the longest time, 121 s, the foam has drained considerably, and the knee no longer is in the field of view of the camera. Thus the rescaled data points do not extend to $s = 0$ as is the case for the profiles at shorter times.

4.3. Pulsed Drainage. We now discuss the one-dimensional dynamics of a pulse with finite liquid volume V_{liq} injected into a foaming tube of cross-sectional area A. We seek a solution to the dimensionless foam drainage equation (36), with the additional constraint that the dimensionless liquid volume be unity, $\int \tilde{\epsilon}\, d\zeta = 1$. This is achieved by choosing the scales

$$T_P = \frac{\delta_\epsilon^{3/2}\gamma^3\mu A^2}{8K_{1/2}(\rho g)^4 L^5 V_{liq}^2} \quad Z_P = \left(\frac{\delta_\epsilon^{1/2}\gamma}{2\rho g L}\right)^2 \frac{A}{V_{liq}} \quad \epsilon_P = \frac{V_{liq}}{AZ_P} \tag{47}$$

The following identities relate the experimentally obtained scaling factors (T_F, Z_P) of forced and free drainage to the pulsed drainage scaling factors (T_P, Z_P):

$$T_P = \left(\frac{AZ_F}{V_{liq}}\right)^2 T_F \qquad Z_P = \frac{AZ_F^2}{V_{liq}} \tag{48}$$

We can compute T_P and Z_P in this way from forced drainage because the same kind of foam is used for both experiments ($L = 0.15$ cm).

The pulse is composed of three sections (see Figure 5c): (i) The first is the *rear* region, where the pulse profile connects to the dry foam above and which is similar to the rear region of free drainage (cf. section 4.2.1). We formally define this region as the range $\zeta = z/Z_P < 0$, although the solutions we present will remain valid for some interval of positive ζ as well. (ii) Next there is the *middle* region, in which the volume fraction grows from $\zeta = 0$ to the peak of the pulse. (iii) Finally, there is the downward moving *front* region below the peak. The latter has characteristics similar to the advancing forced drainage front (see section 4.1). In each of these regions we discuss asymptotic solutions obtained from the node-dominated foam drainage theory and compare them with our experimental measurements.

4.3.1. Rear Region. Here ϵ is small, so we expect surface tension and gravity to be of equal importance, as in the rear region of free drainage. The same self-similar ansatz (37) used before balances all three terms in the foam drainage equation and transforms it into the ODE (38). We expect the upper region of the pulse to develop in this self-similar fashion, and only toward the pulse's peak should deviations from the self-similar behavior occur. In Figure 15 a simulation (open symbols connected by dashed lines) of an initially Gaussian pulse of unit volume and initial width of unity is plotted in (σ, ϕ)space (the variables of (38)). The collapse of the rear region is very good.

Figure 15 also shows experimental data (filled symbols connected by solid lines) for a $V_{liq} = 0.077$ mL pulse plotted in (σ, ϕ) space and illustrates the self-similar behavior of the rear of the pulse. Qualitatively the agreement with the simulations is good; however, on a more quantitative level the length scale Z_P is too large by a factor of about 1.3−2 to achieve excellent agreement. As the deviations seem to increase over time, they are presumably due to the slight differences between the experimentally measured exponents of pulse dynamics (e.g. the pulse maximum coordinate vs time; cf. Figure 11) and the theoretically predicted values. These discrepancies will be discussed further in the following section. Note also that the only free parameter in our theoretical description is $K_{1/2}$, which has been determined from the forced drainage

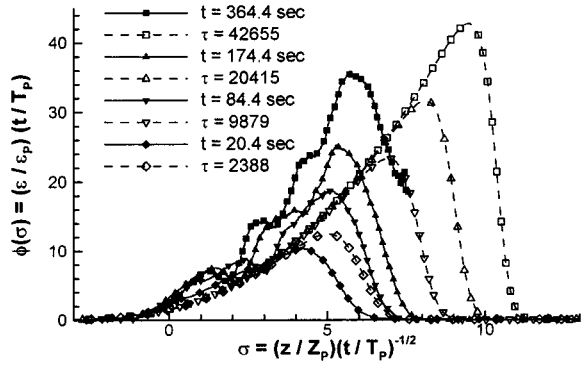

Figure 15. Collapse of the rear regions of simulated and experimental profiles for pulsed drainage using (37). Experimental profiles have filled symbols, and the open symbols show simulations for the corresponding dimensionless times. The liquid volume is $V_{liq} = 0.077$ mL, and the tube area $A = 1.27$ cm^2. The dips before the peaks of some of the experimental profiles can be attributed to the glaring reflection from the UV lamp off the foaming tube.

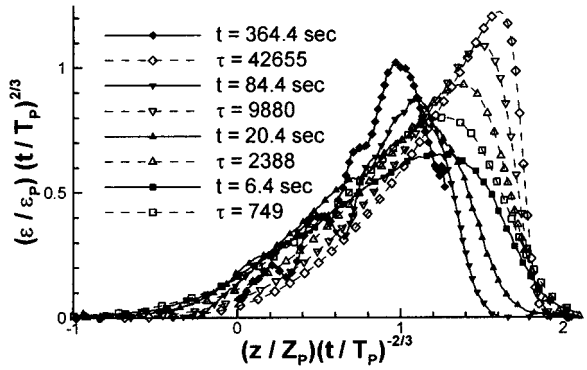

Figure 16. Collapse of pulsed drainage profiles in the middle region where surface tension has been neglected (see (50)). Filled symbols show data for a $V_{liq} = 0.077$ mL pulse; open symbols are the corresponding simulated profiles.

measurements, so that the theoretical predictions for free and pulsed drainage are parameter-free.

4.3.2. Middle Region. While a rescaling as displayed in Figure 15 may put emphasis on the rear region, it is important to realize that the vast majority of the liquid volume resides in the middle region, whose dominance becomes ever larger as time increases. Thus, the gravitational term of the foam drainage equation dominates and the surface tension term may be neglected. As with free drainage, the parabolic profile $\tilde{\epsilon} \approx (2\zeta/3\tau)^2$ then is an approximate solution. The volume constraint, however, limits the extent of the parabola requiring

$$\int_0^{\zeta_{max}} \left(\frac{2\zeta}{3\tau}\right)^2 d\zeta = \frac{4}{27}\frac{\zeta_{max}^3}{\tau^2} = 1 \qquad (49)$$

from which we conclude the power laws

$$\zeta_{max} \approx 3(\tau/2)^{2/3} \qquad \tilde{\epsilon}_{max} \approx (2/\tau)^{2/3} \qquad (50)$$

for the location and height of the pulse peak, respectively. In accordance with these scalings, we use the coordinates $\zeta\tau^{-2/3}$ and $\tilde{\epsilon}\tau^{2/3}$ to collapse experimental and simulated profiles as shown in Figure 16. In the long time limit, the peak location should asymptote toward ζ_{max}, and the peak volume fraction should approach $\tilde{\epsilon}_{max}$. Because the surface tension term was neglected in this approximation, the asymptotic solution of a parabolic profile that abruptly ends at ζ_{max} is approached only slowly, which can be seen in the four simulated profiles.

Table 1. Asymptotic (Long-Time) Approach of the Relations (50) of Peak Position and Peak Height Obtained from a Numerical Simulation (See Text)[a]

τ	10^2	10^3	10^4	10^5	10^6	10^7	∞
d_ϵ	−0.51	−0.53	−0.57	−0.61	−0.64	−0.65	$-2/3$
d_ζ	0.75	0.74	0.72	0.70	0.69	0.68	$2/3$
c_ϵ	0.29	0.33	0.44	0.67	0.93	1.15	1.59
c_ζ	0.74	0.80	0.90	1.10	1.34	1.53	1.89

[a] See (51) for the definitions of d_ϵ, d_ζ, c_ϵ, and c_ζ.

Table 2. Pulse Scales ϵ_P, T_P, and Z_P for Different Injection Volumes V_{liq} Used in the Experiments[a]

V_{liq} (mL)	ϵ_P	T_P (s)	Z_P (cm)	d_ϵ	d_ζ	c_ϵ	c_ζ	τ_{max}
0.25	13.2	8.1×10^{-4}	0.015	−0.56	0.64	0.74	1.16	6.2×10^5
0.14	4.23	2.5×10^{-3}	0.027	−0.61	0.67	0.93	0.92	2.0×10^5
0.077	1.25	8.5×10^{-3}	0.049	−0.57	0.64	0.72	0.96	5.2×10^4
0.022	0.10	0.11	0.17	−0.55	0.63	0.50	0.80	3.6×10^3

[a] The fifth and sixth columns are the measured exponents of the power-law behaviors for the peak height and peak position (see eq 13). The seventh and eighth columns are the prefactors of the peak volume fraction and position in dimensionless units to be compared with the predictions from Table 1. The last column is the duration of the experiment in dimensionless time; $\tau_{max} \equiv$ (maximum experimental time)/T_P.

Although the initial liquid volume distribution is not controlled to be Gaussian in experiment as assumed for the simulation, the comparison with the computations is quite favorable and shows that the data collapse in a fashion similar to the simulation. At short times ($t \sim 10$ s) the agreement between theory and experiment is quite good, and at long times ($t \sim 300$ s) the rescaled experimental pulses are within a factor of 2 of the simulated pulses.

To compare the predictions of (50) to experiment in more detail, we attempt to describe the simulated data by the power laws

$$\zeta_{max} \approx c_\zeta \tau^{d_\zeta} \qquad \tilde{\epsilon}_{max} \approx c_\epsilon \tau^{d_\epsilon} \qquad (51)$$

where d_ζ and d_ϵ are now defined *locally* for a given time τ as the logarithmic derivative of ζ_{max} and $\tilde{\epsilon}_{max}$ with respect to τ, i.e. $d_\zeta = \partial\log(\zeta_{max})/\partial\log(\tau)$ and $d_\epsilon = \partial\log(\tilde{\epsilon}_{max})/\partial\log(\tau)$. Only for very large τ do the simulated peak positions and volume fractions approach the behavior predicted by (50) as shown by Table 1. The convergence of the prefactors to the projected values is even slower than that of the exponents.

Table 2 shows that the measured exponent for the peak position d_ζ stays below the asymptotically predicted value of $2/3$, while the simulated values in Table 1 are all larger than $2/3$ for finite times. This explains the discrepancies seen in Figure 16: as time proceeds, the peak positions, rescaled with the exact theoretical exponent $d_\zeta = 2/3$, drift to the left for the experimental data (with effectively smaller exponents) and to the right for the simulations (which have larger exponents). Since the experimental foam has a permeability of $k(\epsilon) \propto \epsilon^{0.60}$ and not $k(\epsilon) \propto \epsilon^{1/2}$, we expect $d_\zeta = 0.625$.[46] The effect is less pronounced for the scaling of ϵ, where both experiment and theory yield $d_\epsilon > -2/3$. The shift between experiment and theory in the previous Figure 15 can be explained along the same lines: while all peaks move to the right here as time increases (because of the different rescaling), the measured data do so considerably slower than the simulation. Note that the

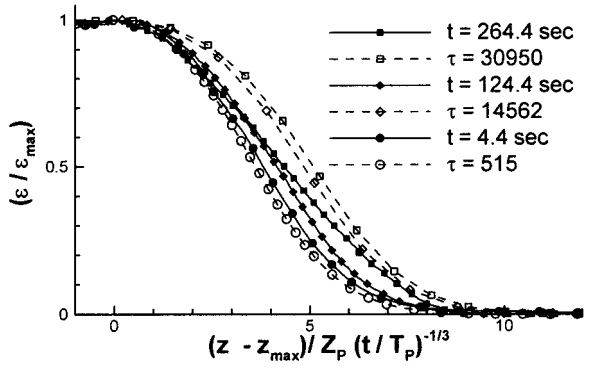

Figure 17. Collapse of the front region of pulsed drainage profiles using (54): experimental data (filled symbols) and simulations (open symbols) at corresponding times. The measurements are for a pulse with $V_{liq} = 0.077$ mL.

simulations also show that the asymptotic behavior is observed only for very long times (Table 1), and in particular, the peak height requires very long times to reach the asymptote $\tilde{\epsilon}_{max} \propto \tau^{-2/3}$. Furthermore, in experiments the initial shape of the pulse is not controlled and most likely not Gaussian. With a more irregular initial condition, it may take longer to establish self-similar behavior. Finally, the experimental foam permeability is measured to be $k(\epsilon) \propto \epsilon^{0.60}$ and not $\propto \epsilon^{1/2}$ which leads to $d_\epsilon \approx -0.625$.[46]

The experimental dimensionless prefactors of Table 2, c_ζ and c_ϵ, are generally about a factor of 2 smaller than the prediction of (50). But for times $\tau \sim 10^5$ even the prefactors for simulations starting with a Gaussian profile are only about half the asymptotic value (see Table 1). This emphasizes the extreme slowness of the asymptotics for the middle collapse.

4.3.3. Front Region. Here we treat the advancing front region of the pulse that stretches from ϵ_{max} to the dry foam below. In dimensionless variables this region is moving downward as $\zeta_{max} \approx 3(\tau/2)^{2/3}$ (see (56)), and we make the ansatz that it is spreading at a rate of τ^λ with $\lambda > 0$. We try a self-similar solution of the form

$$\tilde{\epsilon} = (2/\tau)^{2/3} f(s) \qquad s = \tau^\lambda(\zeta - 3(\tau/2)^{2/3}) \tag{52}$$

Substituting into (36) shows that $\lambda = -1/3$ balances the largest convective term, the gravitational term, and the surface tension term to $O(\tau^{-4/3})$, while two out of the three terms from the time derivative are of magnitude $O(\tau^{-5/3})$ and become negligible at long times. The resulting ordinary differential equation for f is

$$f' - (f^{3/2})' + 2^{-1/3} f'' + O(\tau^{-1/3}) = 0 \tag{53}$$

where the first term stems from the convective time derivative, the second from the advective (gravitational) term, and the third from the diffusive (surface tension) term. We integrate (53) once, which after a substitution of variables, $\tilde{s} = 2^{1/3}s$, and using the boundary condition $f(+\infty) = 0$ gives

$$f(\tilde{s}) - f(\tilde{s})^{3/2} + \frac{df(\tilde{s})}{d\tilde{s}} = 0 \tag{54}$$

which is the same ordinary differential equation that describes the advancing front of forced drainage and whose solution is (31). Figure 17 shows the asymptotic collapse of the bottom of the pulse for both experimental and simulated data using the self-similar ansatz (52). The agreement with simulations is good, although some scatter is present. The solution (31) is indistinguishable from the longest time simulation.

5. Concluding Remarks

We have developed a new method for measuring the liquid volume fraction of foams using fluorescence. It is possible to obtain forced drainage data spanning more than two decades in volume fraction using this technique and extract power-law behavior for the speed and width of the forced drainage wave. For free drainage we measured dynamics over ~100 s, and for pulsed drainage we were able to track the dynamics up to ~500 s.

A generalized foam drainage equation has been derived which takes into account the contributions to viscous damping originating from flow in the nodes as well as in the channels. The foam is modeled as a porous medium with a permeability that varies dynamically with the liquid volume fraction. The foam permeability is governed by the contributions to viscous dissipation in the channels and nodes of the liquid network.

There are two limiting cases of this generalized equation: one with a no-slip interface boundary condition, which is the assumption of the original foam drainage equation, and one with a no-stress (ideally mobile) interface. The former, where dissipation is channel-dominated, is consistent with experimental results from publications by Weaire and co-workers.[8,20,34] The latter, for which nodes dominate the dissipation, agrees very well with all the measurements presented here using SDS surfactant, as well as earlier measurements using Dawn dish detergent.[5]

The measured permeability of the foam in the present experiments has a power-law behavior somewhat different from the node-dominated model ($k \propto \epsilon^{0.6}$ rather than $k \propto \epsilon^{1/2}$). However, the deviations are small and the node-dominated limit reproduces the results of our forced, free, and pulsed drainage experiments with good accuracy, whereas the channel-dominated theory fails to explain our data. The only free parameter in our treatment of the node-dominated foam drainage model is the permeability prefactor $K_{1/2}$ which is taken from the measured dependence of the front velocity against ϵ for forced drainage; see eq 26. The complex foam geometry prevents us from directly computing $K_{1/2}$, e.g. using a boundary integral method with no-stress boundary conditions. Allowing additional dissipation in the channels would add a component to the permeability and increase the effective exponent of the permeability somewhat (see eq 19), thus coming closer to the experimental results.

The node-dominated drainage model provides a very good description of the front width of forced drainage as well as the universal shape of the ϵ profile (see (31)), onto which all experimental data can be collapsed after proper rescaling.

Free drainage experiments are well described by node-dominated drainage as well. Rescaling coordinates according to the theoretical descriptions derived from the node-dominated foam drainage equation collapses both the rear and transition ("knee") regions of free drainage profiles (see Figures 13 and 14). In the asymptotic long-time limit of free drainage, self-similar coordinates transform the PDEs into ODEs, which have exact or approximate analytical solutions. Note that here, rather than focusing on the amount of liquid drained out of the foam in free drainage, we describe the full dynamics of the liquid volume fraction profiles.

Likewise, self-similar solutions are found for the three scaling regimes of pulsed drainage profiles—the rear,

middle, and front regions. The rear region has similar dynamics to the rear region of free drainage (see (38)), and the front region has a similar shape to the advancing front of pulsed drainage (see (54)). We are able to collapse the experimental data from these regimes onto universal curves for long times (see Figures 15−17). The agreement with theory is good especially when considering that, once $K_{1/2}$ is fixed, no other free parameters are used.

In conclusion, we propose a generalized foam drainage theory of which the existing models are special cases and experimentally find that foam drainage is governed by dissipation in the nodes rather than in the channels, which can be rationalized by assuming a no-stress boundary condition at the gas/liquid interface. In fact, since we are dealing with Newtonian fluids, we would expect that qualitative differences in dynamical behavior, such as different scaling laws, can *only* be attributable to changes in the boundary conditions. Recent experiments by Durand et al.[21] suggest that both limits of the generalized foam drainage equation can be approached for the same system by altering the composition of the surfactant: adding dodecanol to an SDS solution increases the surface viscosity and changes the drainage behavior from node-dominated to channel-dominated. Likewise, performing forced drainage experiments with protein surfactants, we find excellent agreement with the channel-dominated model, which has no free parameters. These results support the validity of a generalized theory of foam drainage, as it has been presented here.

Acknowledgment. We are indebted to A. G. Evans for his guidance and support through the MURI project on Ultralight Materials, ONR Grant No. N00014-1-96-1028. We thank G. McKinley for his helpful experimental suggestions and A. Kraynik, J. Sherwood, J. Eggers, and M. Brenner for many useful discussions.

LA9913147